JOURNAL OF GLACIOLOGY

CAMBRIDGE UNIVERSITY PRESS

THIS MANUSCRIPT HAS BEEN SUBMITTED TO THE JOURNAL OF GLACIOLOGY AND HAS NOT BEEN PEER-REVIEWED.

A method for the measurement of seismic attenuation in polar firn

Journal:	*Journal of Glaciology*
Manuscript ID	JOG-22-0115
Manuscript Type:	Article
Date Submitted by the Author:	26-Oct-2022
Complete List of Authors:	Agnew, Ronan; University of Leeds, School of Earth and Environment Clark, Roger; University of Leeds, School of Earth and Environment Booth, Adam; University of Leeds, School of Earth and Environment Brisbourne, Alex; British Antarctic Survey, IDP SMITH, ANDREW; British Antarctic Survey,
Keywords:	Polar firn, Seismics, Glacier geophysics, Glaciological instruments and methods
Abstract:	We present seismic measurements of the firn column at Korff Ice Rise, West Antarctica, including measurements of compressional- and shear-wave velocity and attenuation. We describe a modified spectral-ratio method of measuring the seismic quality factor (Q) based on analysis of diving waves, which enables us to characterise the attenuative structure of firn in greater detail than has previously been possible. The compressional-wave quality factor, Qp, increases from 20 ± 10 in the uppermost firn to 423 ± 260 between 77 and 86 m depth, and the shear-wave quality factor, Qs, increases from 16 ± 9 in the uppermost

	firn to 100 ± 87 between 49 and 64 m depth. Our modified spectral-ratio method aids the understanding of the seismic structure of firn and benefits characterisation of deeper glaciological targets, being particularly impactful for correcting reflection amplitudes in wide-angle seismic data.

Journal of Glaciology, Vol. , No. , 1

A method for the measurement of seismic attenuation in polar firn

Ronan S AGNEW,[1] Roger A CLARK,[1] Adam D BOOTH,[1] Alex M BRISBOURNE[2], Andrew M SMITH[2]

[1] *University of Leeds, Leeds, UK*

[2] *British Antarctic Survey, Cambridge, UK*

Correspondence: Adam Booth <a.d.booth@leeds.ac.uk>

ABSTRACT. We present seismic measurements of the firn column at Korff Ice Rise, West Antarctica, including measurements of compressional- and shear-wave velocity and attenuation. We describe a modified spectral-ratio method of measuring the seismic quality factor (Q) based on analysis of diving waves, which enables us to characterise the attenuative structure of firn in greater detail than has previously been possible. The compressional-wave quality factor, Q_p, increases from 20 ± 10 in the uppermost firn to 423 ± 260 between 77 and 86 m depth, and the shear-wave quality factor, Q_s, increases from 16 ± 9 in the uppermost firn to 100 ± 87 between 49 and 64 m depth. Our modified spectral-ratio method aids the understanding of the seismic structure of firn and benefits characterisation of deeper glaciological targets, being particularly impactful for correcting reflection amplitudes in wide-angle seismic data.

INTRODUCTION

Investigating the structure of polar firn is important for understanding the response of glaciers and ice sheets to a warming climate. Modelling firn density is necessary for calculating ice sheet mass balance from altimetry measurements (e.g. Wingham, 2000; Alley and others, 2007); and the mechanical properties of firn are key to understanding processes of crevasse formation (e.g. Rist and others, 1996) and, potentially, implications for ice shelf rifting and hydrofracture (e.g. Kuipers Munneke and others, 2015; Hubbard and others, 2016; Kulessa and others, 2019).

Interpreting these physical properties from a seismic dataset requires wavelet velocities and amplitudes to be considered. Methods of measuring seismic velocity are well-developed: seismic velocity can be used as a proxy for density (Kohnen, 1972) and can be used to estimate the thickness of the firn column (e.g. Hollmann and others, 2021). Combined estimates of compressional (P) and shear (S) wave velocities can also be used to evaluate mechanical properties such as Poisson's ratio (King and Jarvis, 2007) and elastic moduli (Schlegel and others, 2019). In contrast, tools for measuring seismic amplitude loss, including that resulting from anelastic attenuation, are less well developed. In glaciological settings, geometrical spreading accounts for the largest part of amplitude loss (Smith, 2007), however attenuation losses are an important consideration. Attenuation is caused by both intrinsic mechanisms (elastic wave energy conversion) and apparent mechanisms (e.g., tuning and scattering); their combined effect is measured using the dimensionless seismic quality factor, or Q.

Measuring Q is desirable for two main reasons. The first is that correcting for attenuation through firn is an essential part of many glaciological measurements of seismic amplitude. These include amplitude-versus-offset measurements, which are important for identifying glacial substrates (e.g. Peters and others, 2007; Peters and others, 2008; Booth and others, 2012; Booth and others, 2016, Horgan and others, 2021), as well as normal-incidence methods (e.g. Smith, 1997; Muto and others, 2019). However, current methods of measuring attenuation do not take into account the complex attenuative structure of firn, and often rely on the presence of multiple reflections from the bed, which are not always present with a sufficient signal-to-noise ratio (e.g. Dow and others, 2013; Muto and others, 2019). Second, because Q is influenced by the physical properties of the propagating medium, measuring it has the potential to give further insight into the physical structure of firn. For example, the relationship between the compressional- and shear-wave quality factors and velocities in sands has been observed to be influenced by fluid saturation (Prasad and Meissner, 1992), so measuring Q in firn may have implications for characterising firn hydrology. Recent observations of complex firn structure (Hollmann and others, 2021) and large ice lenses within the firn column (Hubbard and others, 2016) highlight the need for continued in-situ characterisation of firn and improvement of existing methods.

While the continuous increase in seismic velocity with depth enables the velocity-depth structure to be measured in detail by relatively simple methods such as Wiechert-Herglotz inversion (Herglotz, 1907;

Wiechert, 1910; Slichter, 1932), constraining the attenuation structure is less straightforward. However, advances in glaciological seismic acquisition (e.g. Voigt and others, 2013) make Q analyses increasingly feasible. In this paper, we present a novel method of measuring the depth-dependence of Q from diving waves (downgoing direct waves continuously refracted back towards the surface), combining Wiechert-Herglotz inversion with spectral ratio measurements. We apply the method to data from Korff Ice Rise, West Antarctica, providing a more complete description of the firn's attenuative structure than has previously been possible. Ours are the first measurements of the shear-wave quality factor in firn that we know of.

METHODS

The seismic quality factor

As a seismic wave propagates, it loses energy in three generic ways: geometric spreading, partial reflection at interfaces, and by conversion of kinetic energy to heat due to the internal friction of the propagating medium. The lattermost is termed seismic attenuation, and is quantified using a dimensionless quality factor Q. Q is proportional to the fractional energy loss per wave cycle (Aki and Richards, 2002; Sheriff and Geldart, 1995), with higher Q materials associated with more efficient propagation. A wide range of P-wave quality factors (Q_p) have been measured in both polar ice sheets and mountain glaciers; field-based measurements have ranged from $Q_p = 6 \pm 1$ in warm ice (Gusmeroli and others, 2010), to $Q_p > 500$ in cold polar ice (Bentley and Kohnen, 1976). A dependence of Q_p on temperature has been demonstrated both in the laboratory (Kuroiwa, 1994), and in the field (Peters and others, 2012, using a method by Dasgupta and Clark, 1998). Clee and others (1969) measured both Q_p and the shear-wave quality factor, Q_s, in ice near its melting point, and obtained $Q_p/Q_s \sim 3$. However, to the authors' best knowledge no other measurements of Q_s in glacial ice or firn have been reported.

Attenuation measurements have been made across various depth ranges, with some authors measuring Q over the entire ice column from the spectra of pairs of primary/multiple reflections (e.g. Robin, 1958; Bentley, 1971; Jarvis and King, 1993; Booth and others, 2012). Others have measured Q within narrower depth ranges, either by using strong basal and englacial reflections (e.g. Jarvis and King, 1993, Peters and others, 2012) or by measuring the amplitude decay of the direct P wave in a vertical seismic profile (Booth and others, 2020). Q_p has been measured in the uppermost ice of a snow-free glacier (Gusmeroli and others, 2010), and at a single depth at the base of the firn column (Peters, 2009); however little attention has been paid to the depth-dependence of attenuation at intermediate depths in the firn column, and so far measurements of the shear wave attenuation properties of firn are absent. Measurements of Q_p and Q_s are therefore desirable to provide further insight into the structure of the firn itself, and improve the capacity for shear-wave measurement that is extended by 3-component seismic acquisitions.

In this study, we combine measurements of continuously refracted seismic waves with those from basal reflection/source ghost pairs in order to build up a more complete model of the depth dependence of Q_p and Q_s in the firn than has previously been possible.

Field site and data acquisition

Korff Ice Rise (KIR) is located in the Weddell Sea region of West Antarctica, surrounded by the Ronne Ice Shelf (Figure 1). The ice is 530 ± 5 m thick at the divide (the boundary between ice flow directions), with flow velocity < 10 m/a (Kingslake and others, 2016, Brisbourne and others 2019). Previous authors have reported evidence of ice flow reorganisation from observations of Raymond arches (Kingslake and others, 2016) and ice fabric (Brisbourne and others, 2019). Brisbourne and others (2019) reported a crystal orientation fabric above 200 m depth consistent with current ice flow, but a fabric below 230 m depth instead consistent with previous ice flow from the south. KIR therefore may provide insights into the flow history of the ice in the Weddell sea region.

Seismic data were acquired in January 2015 along a line parallel to the ice divide. To measure the P- and S-wave velocities at shallow depths, a line of vertically-oriented georods (Voigt and others, 2013) was deployed with offset intervals progressively increased: 2.5 m between offsets of 2.5 m and 25 m, 5 m to 50 m and 10 m thereafter to a maximum offset of 980 m. A detonator was used as the seismic source, and 2 s of data were recorded with a 16 kHz sampling rate. We use data recorded in this layout to invert for seismic velocities.

For the P-wave attenuation measurements, we use data from a line of vertically oriented georods at 10 m spacing, installed between 30 m and 1940 m offset, with a 150 g explosive source placed at the surface. To record shear motion for the S-wave attenuation measurements, georods were laid radially at intervals of 20 m between 30 m and 1930 m. A buried 600 g explosive source was used to produce shear waves (near-to-source P-to-S converted waves resulting from the nonuniform structure of shallow firn). These data were recorded with an 8 kHz sampling rate. Figure 2 shows aggregated shot gathers from vertical and radially oriented georods, with visible primary, multiple, ghost and diving wave phases. The survey layout used for each measurement is summarised in Table 1.

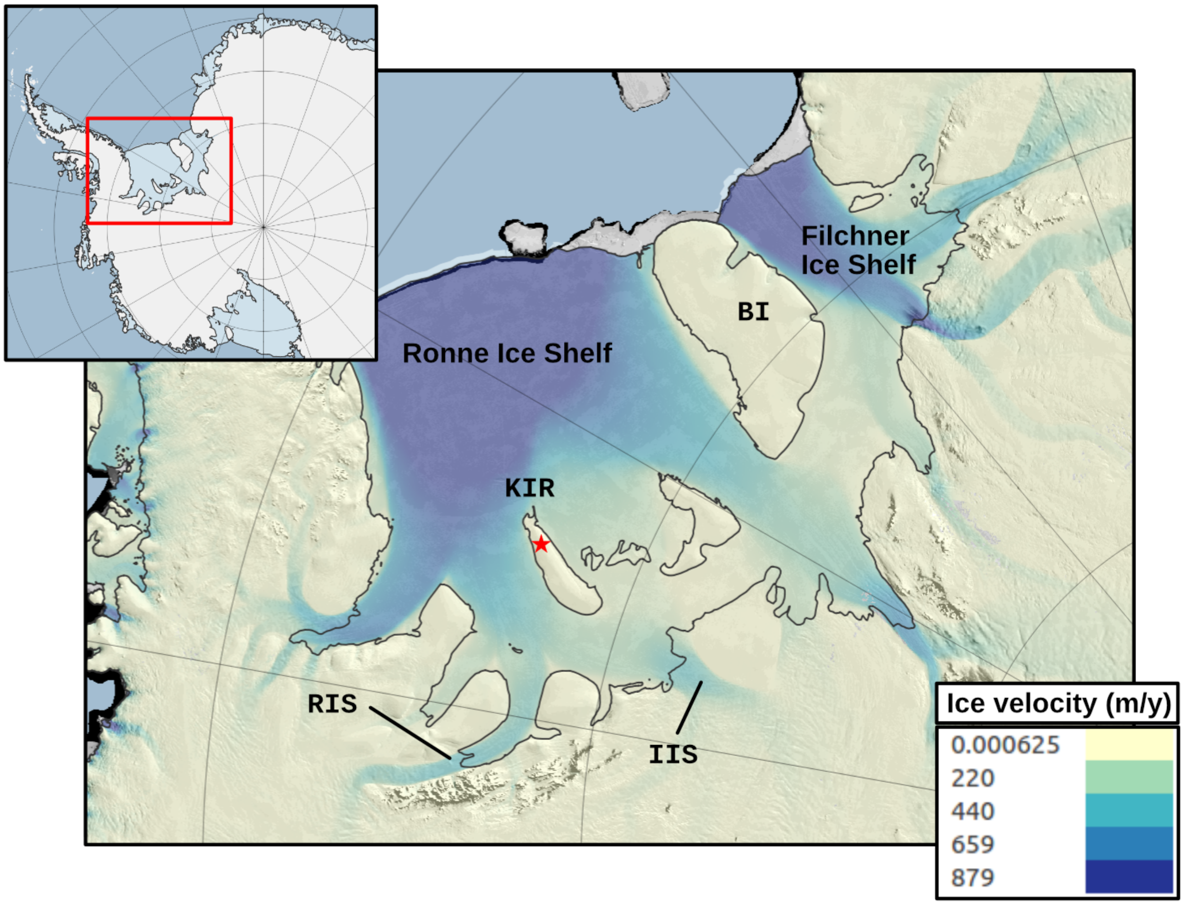

Fig. 1. Location of the field site (red star) on Korff Ice Rise in the Ronne Ice Shelf. Rutford and Institute ice streams are marked, along with Berkner Island (BI). Inset shows the location within Antarctica. MODIS imagery (Scambos and others, 2007) is overlain by MEaSUREs flow velocities (Rignot and others, 2011; Mouginot and others, 2012; Mouginot and others, 2017; Rignot and others, 2017), accessed through Quantarctica (Matsuoka and others, 2021).

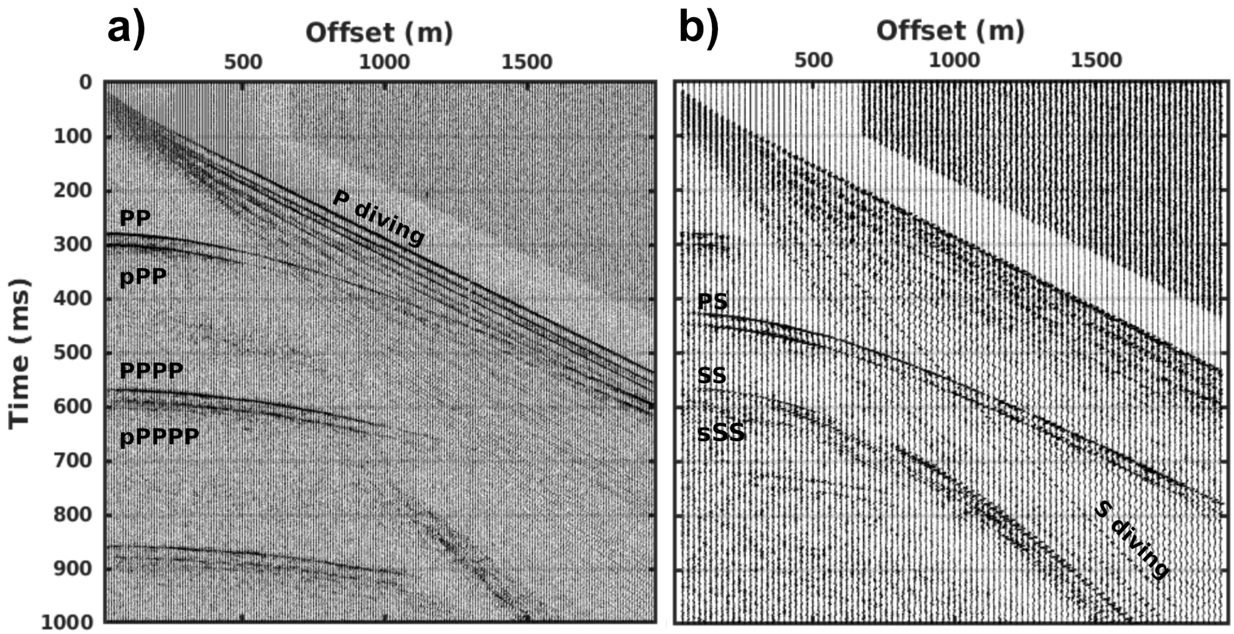

Fig. 2. Aggregated shot gathers in the a) vertical and b) radial directions, with automatic gain control applied for inspection only. Primary reflections (PP, SS) and their surface ghost reflections (pPP, sSS) are clearly visible, as well as multiples and their ghosts (PPPP, pPPPP), a converted wave reflection (PS), and the P and S diving waves.

Table 1. Summary of the survey layout used for each of the velocity and attenuation measurements.

Measurement	Acquisition
V_p, V_s	Expanding survey from 2.5 m to 980 m, detonator only at surface. 16 kHz sampling (short offset refraction). Used to pick short offset ($<$ 100 m) travel times for V_s.
Q_p diving-wave spectral ratio method (layer stripping)	10 m spread at 30 m - 710 m, 150 g surface shot. 16 kHz sampling (far offset refraction).
Q_p in uppermost firn from source ghost	10 m spread at 30 m - 200 m, 150 g shot buried at 20 m depth. 8 kHz sampling (reflection survey).
Q_s layer stripping, Q_s in uppermost firn from source ghost	20 m spread at 30 m - 950 m, 600 g shot buried at 20 m. 8 kHz sampling. Also used to pick S-wave arrivals for WHI at $>$ 200 m, with a buried shot correction applied. Traces up to 100 m used for source ghost measurement.

Spectral ratio method

Seismic attenuation is routinely measured using the spectral ratio method (Teng, 1968, Båth, 1974). Usually the method measures the difference in frequency content of a propagating wavelet at different locations on an otherwise collinear path; we have used a modified method which takes advantage of the firn's continuous velocity gradient and the resulting diving wave paths. The amplitude spectrum $S(f, r)$ of a seismic wavelet of frequency f which has propagated a distance r with no transmission or reflection at interfaces is given by:

$$S(f, r) = S_0(f)G(r)e^{-a(f)r} \tag{1}$$

where $S_0(f)$ is the initial spectrum, $G(r)$ describes geometric spreading and a is the attenuation rate, related to Q by $a = \pi f/Qv$ at frequency f and velocity v. The spectral ratio method compares the spectrum $S_1(f)$ of a wavelet to that of a second wavelet $S_2(f)$, which travels for an additional time δt. The logarithmic ratio of the spectra is

$$\ln \frac{S_2(f)}{S_1(f)} = \frac{-\pi\delta t}{Q} f + \text{constant} \tag{2}$$

Linear regression of the spectral ratio's logarithm against frequency allows a measurement of Q to be made from the slope $m = -\pi\delta t/Q$ (figure 3). We ignore non-physical negative Q results throughout, and consider these to be a result of poor signal-to-noise ratios resulting from problems with individual receiver coupling.

Here we use the commonly adopted assumption that Q is independent of frequency (Kjartansson, 1979). Measured, or effective Q, is the sum of intrinsic and scattering contributions (O'Doherty and Anstey 1971, Schoenberger and Levin 1974). We assume a low-loss formulation and definition of Q (e.g. O'Connell and Budiansky, 1978; Toverud and Ursin, 2005) and a non-dispersive velocity (Kjartansson, 1979; Liner, 2012); we also assume that Q is isotropic. These simplifications are appropriate for the target in question.

Layer stripping method

For the purposes of this method, we represent the firn column as a sequence of layers of uniform Q; the stated quality factor for an individual quasi-layer describes the aggregated effect of attenuation over a defined vertical interval. *Layer stripping* is the name we give to the process by which the quality factor of

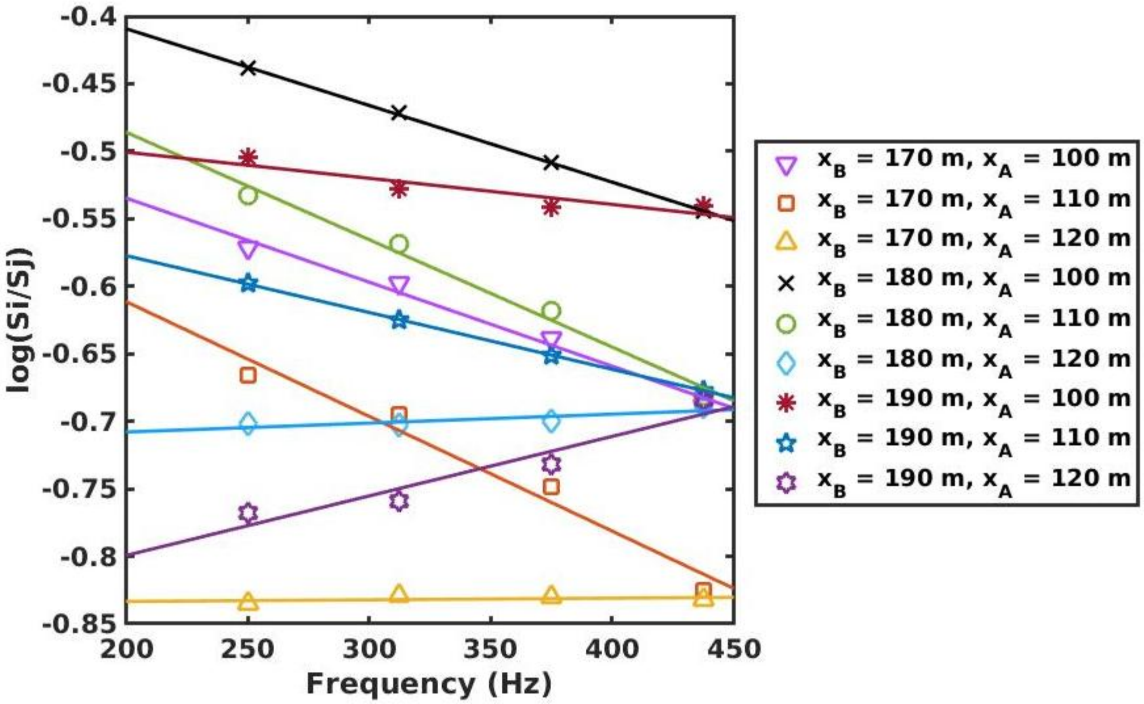

Fig. 3. Examples of logarithmic spectral ratio gradients of diving P waves for a layer in the firn between 25 and 40 m. x_A and x_B are the source-receiver offsets. The spectral ratios are linear within the chosen bandwidth of $200 - 450$ Hz. Positive gradients, which imply the non-physical result of $Q < 0$, are ignored, and assumed to result from poor receiver coupling. Here, the receiver at 190 m offset consistently produces positive gradients and spectra from this receiver would not be used in the final calculations.

an individual quasi-layer in the firn is calculated. This combines spectral ratio measurements of wavelets passing through that layer with an evaluation of the cumulative attenuation through all overlying layers.

The attenuation in the firn column is measured by considering spectral ratios of refracted diving waves (Hepburn, 2016; Alsuleiman, 2018; Crane and others, 2018), which are present due to the continuous velocity increase in the firn column. This method is combined with Wiechert-Herglotz inversion (WHI: Herglotz, 1907; Wiechert, 1910; Slichter, 1932). WHI is designed for seismic velocity profiles which increase smoothly and continuously with depth, assumes 1-D wave propagation, and has been widely described for application to firn velocity modelling (e.g. Kirchner and Bentley, 1990; Jarvis and King, 1993; King and Jarvis, 2007; Horgan and others, 2011; Schlegel and others, 2019; Hollmann and others, 2021). We follow the formulation of the WHI method due to Kirchner and Bentley (1990), and estimate uncertainties in P- and S-wave velocities by applying Gaussian perturbations to wavelet travel times before Wiechert-Herglotz inversion, repeating the process to obtain distributions of velocities as a function of depth. We then calculate the mean and standard deviation of the output distributions to obtain velocity-depth curves for ray tracing. Poisson's ratio, σ, is calculated from the P- and S-wave velocities, V_p and V_s, using the equation

$$\sigma = \frac{V_p^2 - 2V_s^2}{2(V_p^2 - V_s^2)} \tag{3}$$

Figure 4(a) shows diving waves A and B arriving at receivers R1 and R2, having passed through different portions of the firn column. We trace these rays to find their depths of maximum penetration, and interpret layers of uniform Q between these depths, discretising what we assume to be a gradual change in attenuative properties with depth as the firn compacts. The attenuated time t^*, defined as $t^* = t/Q$, is cumulative along each ray (Carpenter, 1966); i.e. for a ray which travels through n layers:

$$t^*_{\text{ray}} = \sum_{i=1}^{n} t^*_i = \sum_{i=1}^{n} \frac{t_i}{Q_i} \tag{4}$$

where t_i is the time a ray spends in layer i, and Q_i is the quality factor in that layer. A wavelet's attenuated time is not measured directly; however, the difference in t^* between two wavelets, δt^*, can be measured from their spectral ratio gradient m, via the relation $m = -\pi \delta t^*$. Ray-tracing is used to determine the time each ray spends in each layer; combined with the measured spectral ratio gradients, this is used to calculate Q in each successive layer. Q_n in layer n is calculated using the spectral ratio gradient of two rays A and B, which penetrate to the bottom of layers $n-1$ and n, respectively:

$$Q_n = t_n^B / \left[\frac{-\pi}{m^{B,A}} + \sum_{i=1}^{n-1} \frac{t_i^A - t_i^B}{Q_i} \right] \tag{5}$$

Here, the superscripts denote the ray and the subscripts denote the layer; i.e., Q_n is the quality factor in layer n, t_i^A is the time ray A spends in layer i, and $m^{B,A}$ is the gradient of the spectral ratio $S^B(f)/S^A(f)$. A derivation of this equation is given in the appendix.

It is apparent from equation (5) that the calculation of Q in each successive layer depends on the calculation of Q in all of the shallower layers. For this reason we refer to the method as 'layer stripping'. This method requires Q in the uppermost layer to be known before the others can be calculated; we measure this using the first multiple bed reflection and its source ghost, described below.

In principle, an attenuation-depth profile as smooth as the velocity-depth profile could be constructed using each successive offset pair; however, in practice, a vertical interval must be thick and/or attenuative enough that its Q contribution is detectable above noise. To obtain more robust results, we use clusters of adjacent traces which penetrate near to the depth of our defined layers (figure 4(a)). We select traces which have a good signal-to-noise ratio, and which produce stable spectral ratio gradients for a range of bandwidths, over which the spectral ratio gradient is constant and the spectra are free from notches caused by destructive interference. We then choose a bandwidth based on inspection of individual spectra. Stable spectra were observed over the frequency ranges listed in table 2; the spectral ratios were measured over these bandwidths.

We construct a 5-layer Q_p model based on available stable spectra with sufficiently large offset differences for a reliable Q_p measurement to be made. Due to the larger spacing between radial georods, and consequently the reduced number of available traces with stable spectra, we construct a 3-layer Q_s model.

Source ghost and multiple measurements

$Q(z)$ profiles output from layer stripping reveal relative variations, and evaluating absolute values requires Q in the shallowest layer to be constrained. Our data were acquired with a buried shot (20 m depth) and hence contain a source ghost. Figure 4b shows the ray paths of the primary bed reflection and its normal incidence source ghost (we take rays with incidence angles $< 10^o$ as normal, following Smith, 2007), which we use to calculate Q_s at the surface, assuming a shallowest layer of 20 m thickness which corresponds to the source depth. The spectral ratio gradient m for these two wavelets can be used with the equation

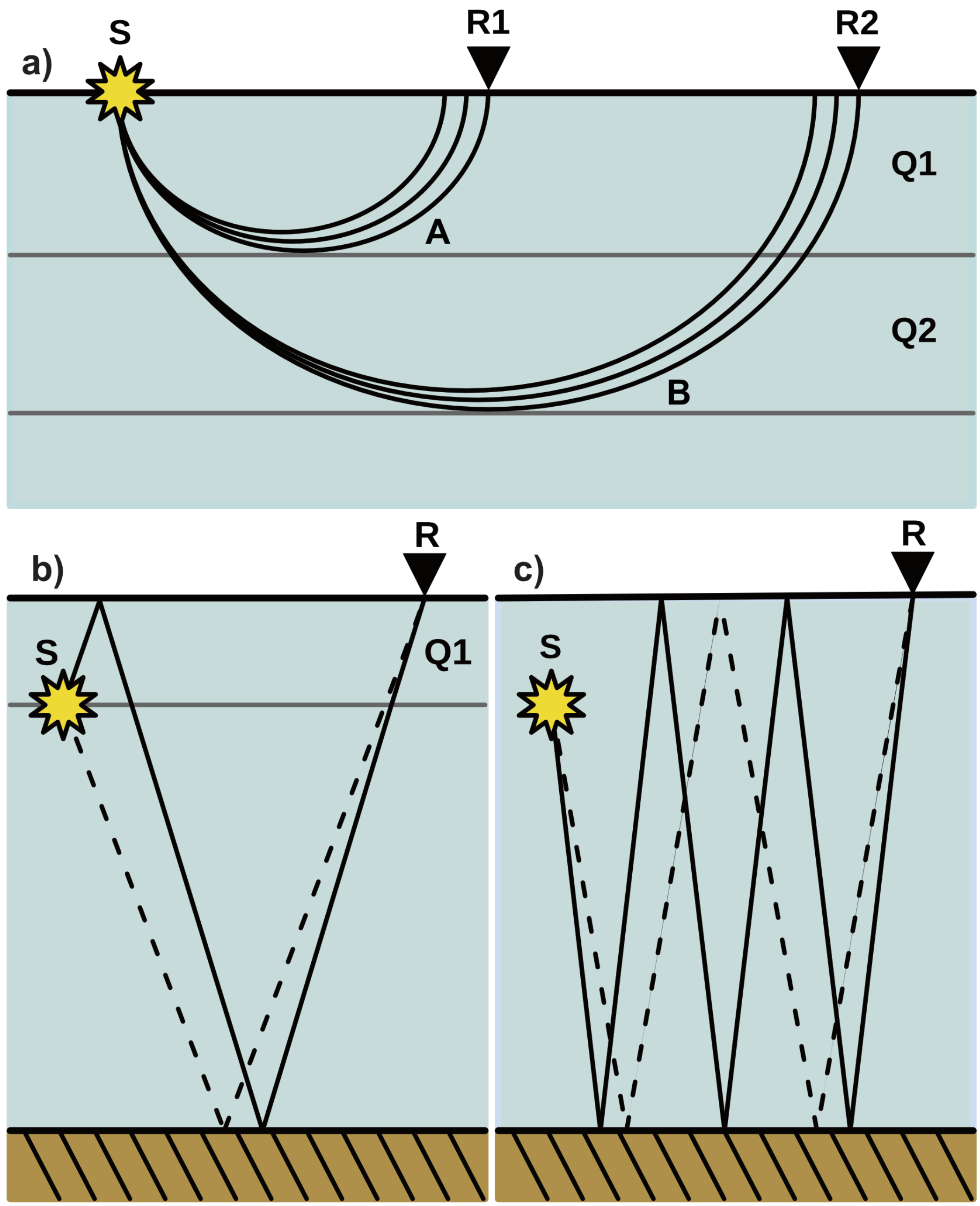

Fig. 4. a) Diving waves travelling between source S and receivers R1, R2. We define layers of constant Q as shown. From the 6 rays shown, we calculate all 9 combinations of spectral ratios and their associated 1/Q, before averaging to obtain a more robust 1/Q measurement. We take the bottoming depth of the deepest ray in a group to be the layer boundary. b) The spectral ratio of the primary reflection (dotted, PP or SS) and surface ghost (solid, pPP or sSS) is used to calculate Q in the uppermost layer. c) The 1st multiple (dotted, PPPP) and 2nd multiple (solid, PPPPPP) are used to independently measure effective Q across the glacier's entire depth. Note that this is schematic, and b) and c) do not show refraction of ray paths due to the firn's velocity gradient.

Table 2. Frequency ranges used for each spectral ratio measurement

Measurement	Frequency range (Hz)
Q_p layer stripping	200 - 450
Q_s layer stripping	100 - 350
Q_p in uppermost layer (source ghost)	200 - 450
Q_s in uppermost layer (source ghost)	100 - 250
Q_p from critical refraction	200 - 450
Q_s from critical refraction	200 - 450
Q_p from first and second multiples	100 - 350

$Q = -\pi \delta t / m$ to calculate Q. In the P-wave record, amplitudes of the basal reflection are clipped at near-normal incidence so Q_p is instead calculated from the spectral ratio of the first multiple (figure 4c, dashed line) and its ghost.

Stochastic error analysis

To estimate the propagation of errors through the layer stripping measurement, we implement a stochastic framework of error analysis. After Q_i is calculated for layer i, a Gaussian perturbation is applied to $1/Q_i$ consistent with the uncertainty on the spectral ratio slope, and this perturbed Q_i is used to calculate the Q_{i+1} of the next layer. We repeat this process 10,000 times to obtain a large number of credible models to analyse statistically. In order to ensure that each generated $Q(z)$ model is physically plausible, we assume two conditions, and accept only models which satisfy these. We require that Q increases with depth (i.e., $Q_{i+1} > Q_i$), and that $Q > 0$ always. We assume that the uncertainty is dominated by the spectral ratios, and that the uncertainty from the travel-time measurement is comparatively small. While these assumptions do not allow all theoretically possible results, we consider them necessary in order to obtain a large enough number of usable models from which statistics can be robustly calculated, given our computational constraints. All statistics are computed from distributions of the quantity $\rho = 1/Q$, and results and uncertainties are quoted as the mean and standard deviation of the output distributions. The uncertainty in Q is then derived from $\epsilon_Q = \epsilon_\rho / \rho^2$, where ϵ_Q is the error in Q and ϵ_ρ is the error in ρ (Topping, 1972).

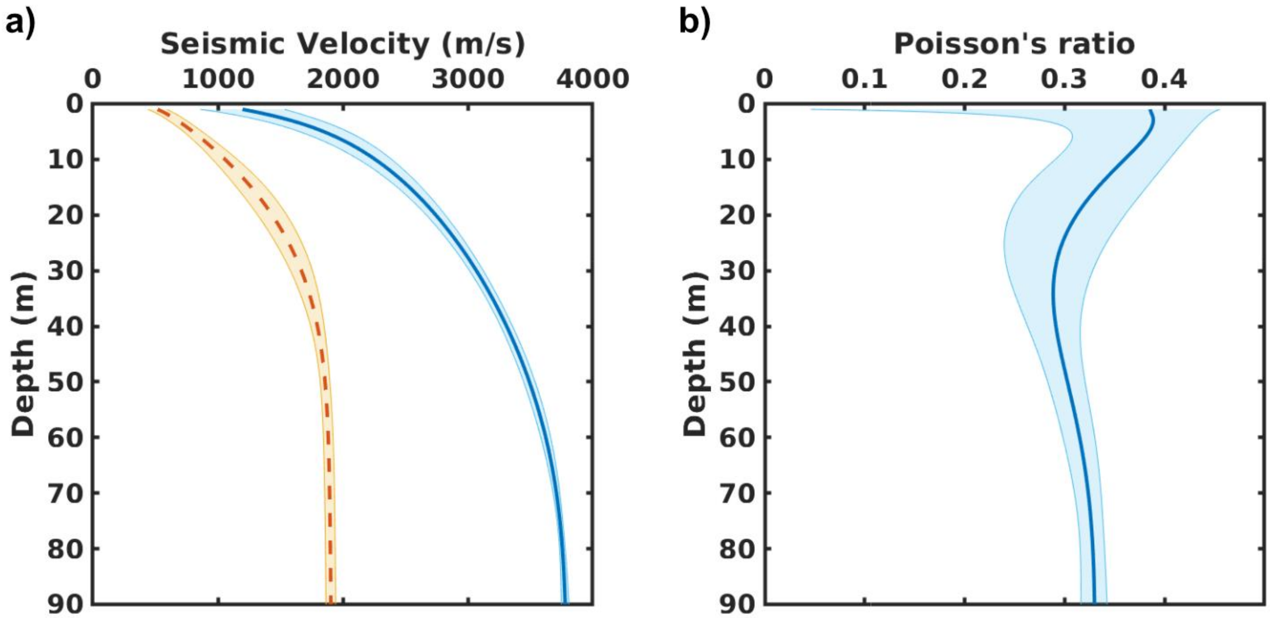

Fig. 5. a) Results from Wiechert-Herglotz inversion, showing the depth-dependence of seismic P-wave (blue solid line) and S-wave (red dashed line) velocity. b) Poisson's ratio as a function of depth in the firn column. Shaded areas indicate uncertainties.

RESULTS

WHI yields velocity-depth models as shown in figure 5a. The P- wave velocity increases with depth from 1200 ± 340 m/s at 1 m depth to 3779 ± 30 m/s at 90 m depth. V_s increases from 517 ± 76 m/s at 1 m depth to 1891 ± 40 m/s at 66 m depth. For our Poisson's ratio calculations, we assume that V_s does not increase further with depth. We see a maximum of Poisson's ratio of $0.39^{+0.05}_{-0.1}$ at 3 m, and a decrease to $0.29^{+0.03}_{-0.04}$ at 34 m, followed by a further increase to 0.330 ± 0.01 at 90 m.

From the first multiple/ghost measurement, we find $Q_p = 21 \pm 12$ and $Q_s = 19 \pm 16$ for the upper 20 m of the firn. The results of our layered-model computation in combination with stochastic error analysis are shown in figures 6 and 7. Figure 6 shows Q_p increasing to 167 ± 96 between 55 and 77 m depth, while Q_s increases to 100 ± 87 between 49 m and 64 m depth. Tables 3 and 4 show the results for intermediate depths for Q_p and Q_s, respectively.

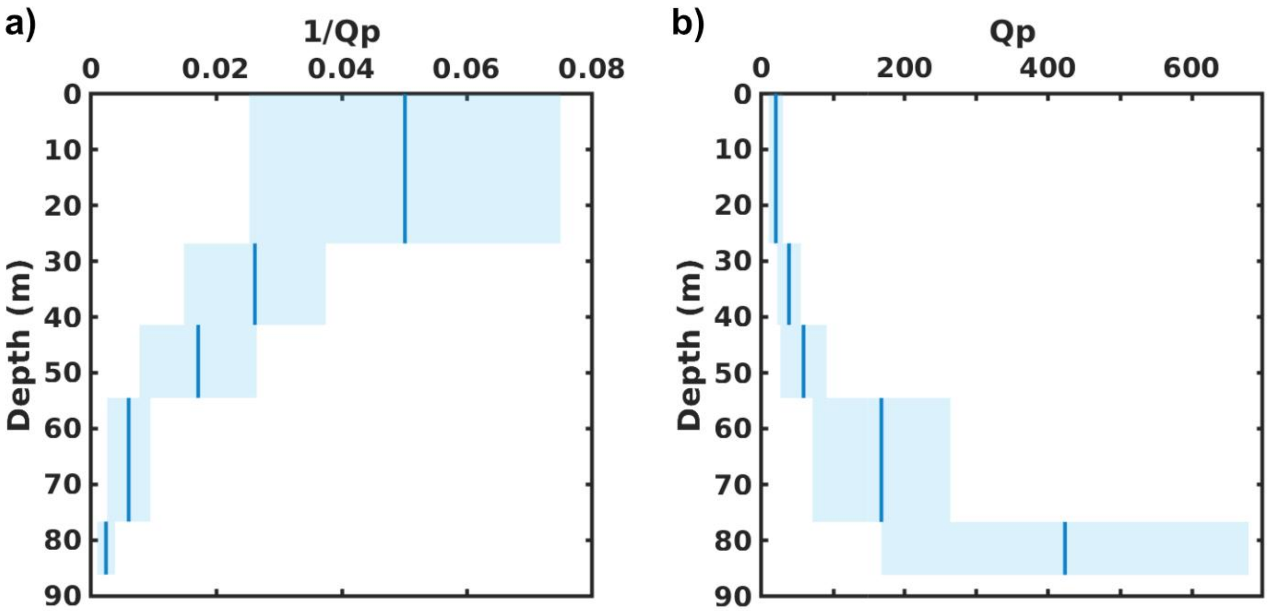

Fig. 6. a) Mean of 1/Qp versus depth for a five-layer model. Shaded area represents the standard deviation of sampled models. b) Qp model resulting from statistical analysis of 1/Qp data.

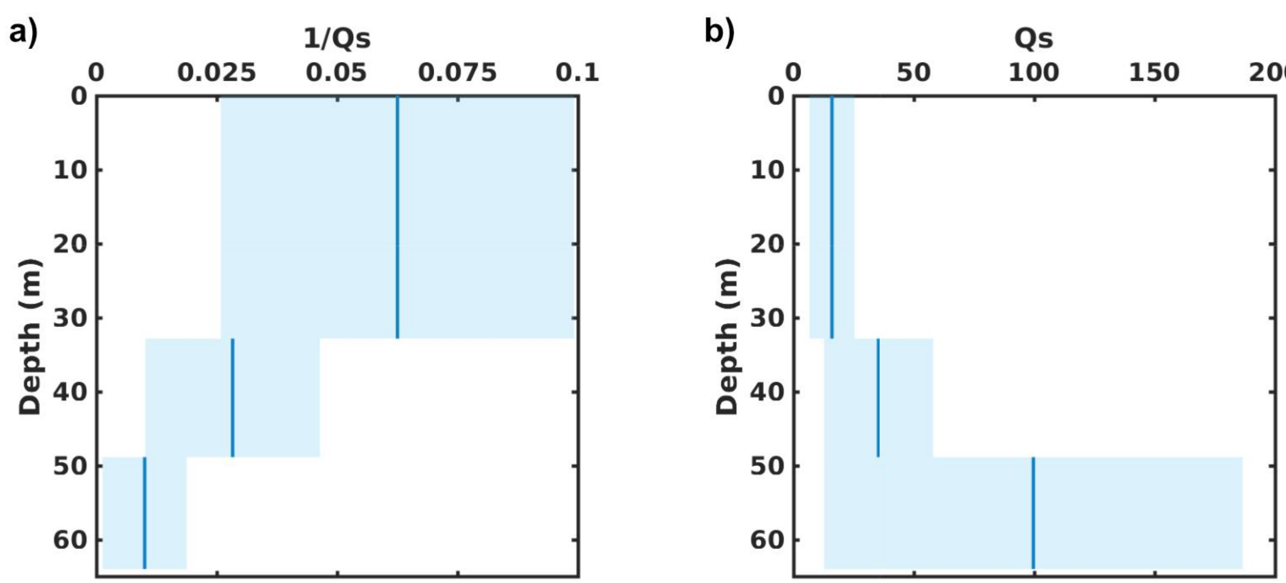

Fig. 7. Qs results. a) Mean 1/Qs for each layer with standard deviation shaded. b) Qs model resulting from 1/Qs calculations.

Table 3. Q_p model, shown in figure 6(b)

Depth (m)	Q_p
0-27	20 ± 10
27-41	38 ± 17
41-55	59 ± 32
55-77	167 ± 96
77-86	423 ± 260

Table 4. Q_s model, shown in figure 7(b)

Depth (m)	Q_s
0-33	16 ± 9
33-49	35 ± 23
49-64	100 ± 87

DISCUSSION

We have shown an effective method of deriving the velocity and attenuation profiles through firn and ice, including a robust evaluation of uncertainties.

Our measurements of seismic velocity and Poisson's ratio are consistent with recent measurements by Schlegel and others (2019) and Kulessa and others (2019), which show V_p continuing to increase beyond the depth of maximum V_s. We observe a maximum in Poisson's ratio at ~ 3 m, which is potentially related to the change in densification mechanism from grain reorganisation to recrystallisation. The minimum Poisson's ratio we observe occurs at $\sim$ 34 m, which is close to the pore close-off depth of 46 ± 1 m calculated from the empirical V_p-density relationship by Kohnen (1972). However, these measurements are inconsistent with those of Kirchner and Bentley (1979), King and Jarvis (1997), and Sayers (2021); further measurements are needed to more fully understand links between firn densification processes and its elastic properties. Due to the large uncertainties and broad geographical (climatological) spread of these studies we do not investigate features in this curve any further.

To validate the layer stripping approach to calculating Q, we can compare results with an independent measurement from critically refracted waves. Critical refractions occur at the point at which seismic velocity stops increasing. At this depth, Q can be straightforwardly measured using the log spectral ratio of two critically refracted arrivals and $Q = -\pi\delta t/m$. Using this method gives $Q_p = 458 \pm 240$ at 90 ± 14 m and $Q_s = 81 \pm 50$ at 66 ± 29 m. Comparison with Q_p and Q_s obtained from layer stripping at similar depths (figs. 6 and 7) shows consistency between the two methods.

We observe Q_p and Q_s to be similar in the uppermost portions of the firn column. The similarity in shallow firn ($Q_p/Q_s = 1.25 \pm 2$ in the uppermost $\sim$ 30 m) contrasts with the earlier measurement of $Q_p/Q_s = 3$ in ice (Clee and others, 1969), highlighting the need for more detailed characterisation of firn's seismic properties. Our method works only to the depth of critical refraction, so it is not possible to say whether Q_s continues increasing as Q_p does to $\sim$ 90 m.

Q_p is commonly measured using methods based on the spectral ratio of primary reflections and their corresponding multiples (e.g. Booth and others, 2012). In our P-wave record, the primary reflection is clipped at close to normal incidence, so we use the spectral ratios of normal incidence first and second multiples (Figure 4(c)). This gives the effective Q through the whole glacier, including the firn and its underlying ice. The signal-to-noise ratio of S-wave multiples was not sufficient to repeat this for Q_s.

Measured using this method, the effective Q_p from surface to bed is $Q_p = 234 \pm 160$. For a normal incidence reflection, our layered Q model has an effective Q_p of 127 ± 67, assuming that Q_p does not increase below the firn column. These measurements show some spread, but given the large uncertainty on the multiple-based measurement, we consider them to be consistent with one another.

A key motivation for measuring Q in the firn is the need to compensate for Q losses when the amplitude of seismic waves is of interest, for example when using amplitude-versus-offset (AVO) analysis to identify a subglacial material (e.g. Peters and others, 2008, Booth and others, 2012). We highlight the significance of our approach by considering what difference a layered Q model would make to an AVO measurement versus a model which assumes a uniform Q throughout the whole glacier. We do this by producing a synthetic AVO gather of a reflection from 530 m thick ice over bedrock, dominant frequency 200 Hz, which incorporates our detailed firn-Q model and velocity model. We then pick the amplitudes, and recalculate the bed reflection coefficient using a) our detailed Q model, assuming that Q is uniform from our deepest measurement to the glacier bed, and b) the assumption that $Q = 127$ everywhere. The value $Q = 127$ is chosen to ensure that the attenuated time t^* is the same at normal incidence for both Q models. This means that any differences observed in the corrected bed reflectivities arise from the use of a different model to correct for attenuation losses, and not from measurement errors, as would be the case if we had used a measurement from multiples, for example. Figure 8(a) shows the angular dependence of the applied attenuative correction, $\exp(\pi f t^*)$, and figure 8(b) shows the two corrected reflectivity curves. At small incidence angles, the difference is very small compared with typical signal-to-noise ratios (and by definition of t^*, zero at normal incidence), so the uniform-Q assumption is appropriate for short survey geometries. However at large incidence angles, using the uniform-Q method would under-correct the amplitudes (by a factor of ~ 2 at 60^o). For this reason we consider correction with a layered firn Q model to be preferable for very long-offset surveys (where incidence angles $> 50^o$).

There are other circumstances in which it would be preferable to choose a layer stripping measurement over a multiple-based one. First, for seismic experiments studying the firn itself, a measurement of Q in the firn is necessary, as clearly it is not valid to assume that Q at shallow depths is the same as the effective Q that would be measured using multiples. Second, thin layering at the ice-bed interface (Booth and others, 2012) can cause interference effects which change the apparent amplitudes of the multiples, making a multiple-based measurement inappropriate. Third, multiples are not always clearly visible in a seismic dataset (e.g. Dow and others, 2013; Muto and others, 2019); in such a case $Q(z)$ would need to be

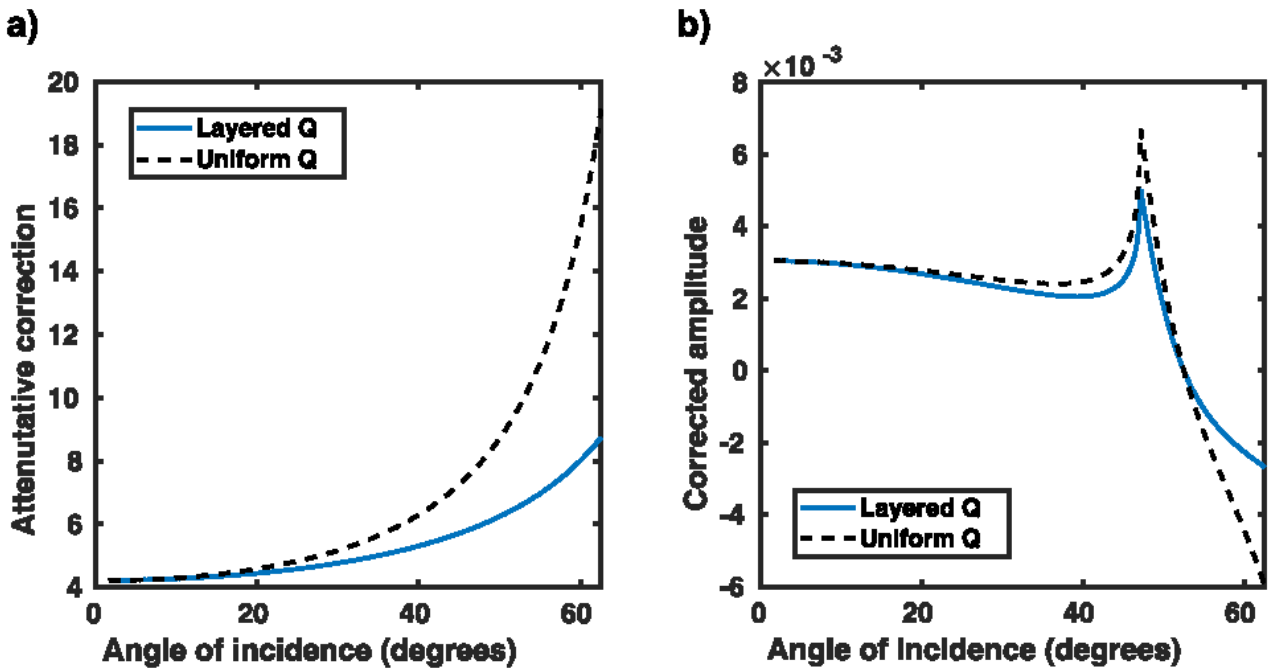

Fig. 8. a) Angular dependence of the attenuative correction applied when correcting synthetic amplitude-versus-offset (AVO) data for geometric spreading and attenuation losses, for a layered Q model (solid blue line), and a uniform-Q assumption (dashed black line). b) Bed reflectivities obtained from synthetic data simulating a P-wave reflection from an ice-bedrock interface. Data are not corrected for synthetic source amplitude and the y-axis is consequently multiplied by a constant. At close to normal incidence, the difference is small, but at 60 degree incidence, there is a factor of ~ 2 difference between the corrected AVO curves.

estimated by layer stripping.

The uncertainty in $Q(z)$ comes mainly from the uncertainty in the spectral ratio gradients. In future, particular care should be taken to ensure consistently excellent receiver coupling if a good measurement of Q is to be obtained.

Our method has potential for improvement. A more detailed model could be produced if more closely spaced, or even all, traces were used, resulting in a model with very thin layers and providing a truer representation of the continuous nature of firn transformation; however, this would require an extremely good signal-to-noise ratio that was not achieved with our dataset. We can make a number of recommendations for acquisition based on the obtained $Q(z)$ profiles for P- and S-waves. First, we recommend a maximum receiver spacing of 10 m. The 20 m spacing used here for the calculation of Q_s limits the number of traces with a sufficiently high signal-to-noise ratio which record (non-critical) diving wave paths. Second, we recommend the use of a dedicated S-wave source (e.g. King and Jarvis, 2007). This would minimise P-wave contamination of observed S-waves. Here, we used a more powerful source to ensure a measurable amplitude of at-source P-to-S converted waves, which resulted in a large degree of clipping at near-offsets, again limiting the number of usable traces, and requiring the assumption of a uniform Q_s down to the maximum penetration depth of the nearest-offset non-clipped diving wave (33 m). We had to make the same assumption for Q_p; however due to the smaller distance between receivers, we were able to assume a uniform Q_p to 27 m. A dedicated S-wave source would not need to be as powerful, reducing clipping and allowing greater detail in the Q_s profile to be observed. However, the main factor limiting our Q_s measurement is the reduced depth penetration of diving S-waves at this site when compared with diving P-waves. In future, the layer stripping method could be combined with multiple-based measurements or those relying on englacial reflections (e.g., Peters and others, 2012) in order to build up a more comprehensive englacial Q-profile; this could be supplemented by a dedicated microspread to resolve detail at very shallow depths (e.g. Gusmeroli and others, 2010).

CONCLUSIONS

We have demonstrated a novel application of the spectral ratio method for the measurement of the seismic quality factor Q in firn, and then applied this method to data from Korff Ice Rise in West Antarctica. We have therefore been able to resolve the attenuative structure of firn in greater detail than has previously been possible; furthermore, to the best of our knowledge, we have made the first measurement of the shear-wave quality factor in firn. Our results show Q_p increasing from 20 ± 10 at the surface to 423 ± 260 between 77 and 86 m depth, while Q_s increases from 16 ± 9 near the surface to 100 ± 87 between 49 and 64 m depth. Our results are consistent with measurements made independently using critically refracted waves. The uncertainty on the spectral ratio gradient dominates over other contributions, showing that (as is typical of seismic attenuation measurements) an excellent signal-to-noise ratio is essential if this method is to be used. In addition to this, we have measured the compressional- and shear-wave seismic velocities and Poisson's ratio. Our results provide a fuller characterisation of firn's seismic properties than has previously been possible, and our methods will aid future seismic investigations of glaciological targets.

ACKNOWLEDGEMENTS

These data were collected as part of the British Antarctic Survey programme Polar Science for Planet Earth with the support of British Antarctic Survey Operations. RSA is supported by the NERC PANORAMA Doctoral Training Partnership.

REFERENCES

Aki K and Richards PG (2002) *Quantitative seismology.* University Science Books, Sausalito, CA, USA

Alley RB, Spencer MK and Anandakrishnan S (2007) Ice-sheet mass balance: assessment, attribution and prognosis. *Annals of Glaciology*, **46**, 1–7 (doi: 10.3189/172756407782871738)

Alsuleiman A (2018) *Measuring seismic attenuation for the firn layer in Antarctica.* Unpublished BSc. Geophysical Sciences dissertation, School of Earth and Environment, University of Leeds

Båth M (1974) *Developments in solid Earth Geophysics: spectral analysis in Geophysics.* Elsevier Scientific Publishing Company

Bentley CR (1971) Seismic Evidence for Moraine within the Basal Antarctic Ice Sheet. In A Crary (ed.), *Antarctic Research Series*, 89–129, American Geophysical Union, Washington, D. C. (doi: 10.1029/AR016p0089)

Bentley CR and Kohnen H (1976) Seismic refraction measurements of internal friction in Antarctic ice. *Journal of Geophysical Research*, **81**(8), 1519–1526 (doi: 10.1029/JB081i008p01519)

Booth AD, Clark RA, Kulessa B, Murray T, Carter J, Doyle S and Hubbard A (2012) Thin-layer effects in glaciological seismic amplitude-versus-angle (AVA) analysis: implications for characterising a subglacial till unit, Russell Glacier, West Greenland. *The Cryosphere*, **6**(4), 909–922 (doi: 10.5194/tc-6-909-2012)

Booth AD, Christoffersen P, Schoonman C, Clarke A, Hubbard B, Law R, Doyle SH, Chudley TR and Chalari A (2020) Distributed acoustic sensing of seismic properties in a borehole drilled on a fast-flowing Greenlandic outlet glacier. *Geophysical Research Letters*, **47**(13) (doi: 10.1029/2020GL088148)

Brisbourne AM, Martín C, Smith AM, Baird AF, Kendall JM and Kingslake J (2019) Constraining Recent Ice Flow History at Korff Ice Rise, West Antarctica, Using Radar and Seismic Measurements of Ice Fabric. *Journal of Geophysical Research: Earth Surface*, **124**(1), 175–194 (doi: 10.1029/2018JF004776)

Carpenter EW, Bullard EC and Penney WG (1966) A quantitative evaluation of teleseismic explosion records. *Proceedings of the Royal Society of London. Series A. Mathematical and Physical Sciences*, **290**(1422), 396–407 (doi: 10.1098/rspa.1966.0058)

Clee TE, Savage JC and Neave KG (1969) Internal friction in ice near its melting point. *Journal of Geophysical Research*, **74**(4), 973–980 (doi: 10.1029/JB074i004p00973)

Crane JM, Lorenzo JM, Shen J and White CD (2018) The competing effects of stress and water saturation on *in situ* Q for shallow (< 1 m), unconsolidated sand, evaluated with a modified spectral ratio method. *Near Surface Geophysics*, **16**(2), 104–117 (doi: 10.3997/1873-0604.2017048)

Dasgupta R and Clark RA (1998) Estimation of Q from surface seismic reflection data. *Geophysics*, **63**(6), 2120–2128 (doi: 10.1190/1.1444505)

Gusmeroli A, Clark RA, Murray T, Booth AD, Kulessa B and Barrett BE (2010) Seismic wave attenuation in the uppermost glacier ice of Storglaciären, Sweden. *Journal of Glaciology*, **56**(196), 249–256 (doi: 10.3189/002214310791968485)

Hepburn D (2016) *Estimation of the seismic attenuation in firn through use of the Wiechert-Herglotz Inversion and spectral ratio methods.* Unpublished MSc. Exploration Geophysics dissertation, School of Earth and Environment, University of Leeds

Herglotz G (1907) Über das Benndorfsche problem der fortpflanzungsgeschwindigkeit der erdbebenstrahlen (on the Benndorf problem of propagation velocity of earthquake rays). *Zeitschrift für Geophysik*, **8**, 145–147

Hollmann H, Treverrow A, Peters LE, Reading AM and Kulessa B (2021) Seismic observations of a complex firn structure across the Amery Ice Shelf, East Antarctica. *Journal of Glaciology*, **67**(265), 777–787 (doi: 10.1017/jog.2021.21)

Horgan HJ, Anandakrishnan S, Alley RB, Burkett PG and Peters LE (2011) Englacial seismic reflectivity: imaging crystal-orientation fabric in West Antarctica. *Journal of Glaciology*, **57**(204), 639–650 (doi: 10.3189/002214311797409686)

Horgan HJ, van Haastrecht L, Alley RB, Anandakrishnan S, Beem LH, Christianson K, Muto A and Siegfried MR (2021) Grounding zone subglacial properties from calibrated active-source seismic methods. *The Cryosphere*, **15**(4), 1863–1880 (doi: 10.5194/tc-15-1863-2021)

Hubbard B, Luckman A, Ashmore DW, Bevan S, Kulessa B, Kuipers Munneke P, Philippe M, Jansen D, Booth A, Sevestre H, Tison JL, O'Leary M and Rutt I (2016) Massive subsurface ice formed by refreezing of ice-shelf melt ponds. *Nature Communications*, **7**(1), 11897 (doi: 10.1038/ncomms11897)

Jarvis E and King E (1993) The seismic wavefield recorded on an Antarctic ice shelf. *Journal of Seismic Exploration*, **2**, 69–86

King EC and Jarvis EP (2007) Use of Shear Waves to Measure Poisson's Ratio in Polar Firn. *Journal of Environmental and Engineering Geophysics*, **12**(1), 15–21 (doi: 10.2113/JEEG12.1.15)

Kingslake J, Martín C, Arthern RJ, Corr HFJ and King EC (2016) Ice-flow reorganization in West Antarctica 2.5 kyr ago dated using radar-derived englacial flow velocities. *Geophysical Research Letters*, **43**(17), 9103–9112 (doi: 10.1002/2016GL070278)

Kirchner JF and Bentley CR (1990) RIGGS III: Seismic Short-Refraction Studies Using an Analytical Curve-Fitting Technique. In CR Bentley and DE Hayes (eds.), *Antarctic Research Series*, 109–126, American Geophysical Union, Washington, D. C. (doi: 10.1029/AR042p0109)

Kjartansson E (1979) Constant Q -wave propagation and attenuation. *Journal of Geophysical Research*, **84**(B9), 4737 (doi: 10.1029/JB084iB09p04737)

Kohnen H (1972) Über die beziehung zwischen seismischen geschwindigkeiten und der dichte in firn und eis. *Zeitschrift für Geophysik*, **38**(5), 925–935

Kuipers Munneke P, Ligtenberg SR, Van Den Broeke MR and Vaughan DG (2014) Firn air depletion as a precursor of Antarctic ice-shelf collapse. *Journal of Glaciology*, **60**(220), 205–214 (doi: 10.3189/2014JoG13J183)

Kulessa B, Booth AD, O'Leary M, McGrath D, King EC, Luckman AJ, Holland PR, Jansen D, Bevan SL, Thompson SS and Hubbard B (2019) Seawater softening of suture zones inhibits fracture propagation in Antarctic ice shelves. *Nature Communications*, **10**(1), 5491 (doi: 10.1038/s41467-019-13539-x)

Kuroiwa D (1964) Internal friction of ice. III : The internal friction of natural glacier ice. *Contributions from the Institute of Low Temperature Science*, **18**, 49–62

Liner CL (2012) *Elements of seismic dispersion: A somewhat practical guide to frequency-dependent phenomena.* Society of Exploration Geophysicists, DISC Series 15

Matsuoka K, Skoglund A, Roth G, de Pomereu J, Griffiths H, Headland R, Herried B, Katsumata K, Le Brocq A, Licht K, Morgan F, Neff PD, Ritz C, Scheinert M, Tamura T, Van de Putte A, van den Broeke M, von Deschwanden A, Deschamps-Berger C, Van Liefferinge B, Tronstad S and Melvær Y (2021) Quantarctica, an integrated mapping environment for Antarctica, the Southern Ocean, and sub-Antarctic islands. *Environmental Modelling & Software*, **140**, 105015 (doi: 10.1016/j.envsoft.2021.105015)

Mouginot J, Scheuchl B and Rignot E (2012) Mapping of ice motion in Antarctica using synthetic-aperture radar data. *Remote Sensing*, **4**(9), 2753–2767 (doi: 10.3390/rs4092753)

Mouginot J, Rignot E, Scheuchl B and Millan R (2017) Comprehensive annual ice sheet velocity mapping using Landsat-8, Sentinel-1, and RADARSAT-2 data. *Remote Sensing*, **9**(4) (doi: 10.3390/rs9040364)

Muto A, Anandakrishnan S, Alley RB, Horgan HJ, Parizek BR, Koellner S, Christianson K and Holschuh N (2019) Relating bed character and subglacial morphology using seismic data from Thwaites Glacier, West Antarctica. *Earth and Planetary Science Letters*, **507**, 199–206 (doi: 10.1016/j.epsl.2018.12.008)

O'Connell RJ and Budiansky B (1978) Measures of dissipation in viscoelastic media. *Geophysical Research Letters*, **5**(1), 5–8 (doi: https://doi.org/10.1029/GL005i001p00005)

O'Doherty RF and Anstey NA (1971) Reflections on amplitudes. *Geophysical Prospecting*, **19**(3), 430–458 (doi: 10.1111/j.1365-2478.1971.tb00610.x)

Peters LE (2009) *A seismic investigation of basal conditions in glaciated regions*. Unpublished PhD thesis, Pennsylvania State University Graduate School

Peters LE, Anandakrishnan S, Alley RB and Smith AM (2007) Extensive storage of basal meltwater in the onset region of a major West Antarctic ice stream. *Geology*, **35**(3), 251 (doi: 10.1130/G23222A.1)

Peters LE, Anandakrishnan S, Holland CW, Horgan HJ, Blankenship DD and Voigt DE (2008) Seismic detection of a subglacial lake near the South Pole, Antarctica. *Geophysical Research Letters*, **35**(23), L23501 (doi: 10.1029/2008GL035704)

Peters LE, Anandakrishnan S, Alley RB and Voigt DE (2012) Seismic attenuation in glacial ice: A proxy for englacial temperature. *Journal of Geophysical Research: Earth Surface*, **117**(F2) (doi: 10.1029/2011JF002201)

Prasad M and Meissner R (1992) Attenuation mechanisms in sands: Laboratory versus theoretical (Biot) data. *Geophysics*, **57**(5), 710–719 (doi: 10.1190/1.1443284)

Rignot E, Mouginot J and Scheuchl B (2011) Ice flow of the Antarctic Ice Sheet. *Science*, **333**(6048), 1427–1430 (doi: 10.1126/science.1208336)

Rignot E, Mouginot J and Scheuchl B (2017) MEaSUREs InSAR-based Antarctica ice velocity map, version 2 (doi: 10.5067/D7GK8F5J8M8R)

Rist MA, Sammonds PR, Murrell SAF, Meredith PG, Oerter H and Doake CSM (1996) Experimental fracture and mechanical properties of Antarctic ice: preliminary results. *Annals of Glaciology*, **23**, 284–292 (doi: 10.3189/S0260305500013550)

Robin G (1958) Glaciology III: Seismic shooting and related investigations. *Norwegian–British–Swedish Antarctic Expedition, 1949–52, Scientific Results*, **5**

Sayers CM (2021) Porosity dependence of elastic moduli of snow and firn. *Journal of Glaciology*, **67**(265), 788–796 (doi: 10.1017/jog.2021.25)

Scambos T, Haran T, Fahnestock M, Painter T and Bohlander J (2007) MODIS-based mosaic of Antarctica (MOA) data sets: Continent-wide surface morphology and snow grain size. *Remote Sensing of Environment*, **111**(2), 242–257 (doi: 10.1016/j.rse.2006.12.020)

Schlegel R, Diez A, Löwe H, Mayer C, Lambrecht A, Freitag J, Miller H, Hofstede C and Eisen O (2019) Comparison of elastic moduli from seismic diving-wave and ice-core microstructure analysis in Antarctic polar firn. *Annals of Glaciology*, **60**(79), 220–230 (doi: 10.1017/aog.2019.10)

Schoenberger M and Levin FK (1974) Apparent attenuation due to intrabed multiples. *Geophysics*, **39**(3), 278–291 (doi: 10.1190/1.1440427)

Sheriff RE and Geldart LP (1995) *Exploration seismology*. Cambridge university press

Slichter LB (1932) The theory of the interpretation of seismic travel-time curves in horizontal structures. *Physics*, **3**(6), 273–295 (doi: 10.1063/1.1745133)

Smith AM (1997) Basal conditions on Rutford Ice Stream, West Antarctica, from seismic observations. *Journal of Geophysical Research: Solid Earth*, **102**(B1), 543–552 (doi: 10.1029/96JB02933)

Smith AM (2007) Subglacial bed properties from normal-incidence seismic reflection data. *Journal of Environmental and Engineering Geophysics*, **12**(1), 3–13 (doi: 10.2113/JEEG12.1.3)

Teng TL (1968) Attenuation of body waves and the Q structure of the mantle. *Journal of Geophysical Research (1896-1977)*, **73**(6), 2195–2208 (doi: https://doi.org/10.1029/JB073i006p02195)

Topping J (1972) *Errors of observation and their treatment*. Chapman and Hall Science paper back, 4th edn.

Toverud T and Ursin B (2005) Comparison of seismic attenuation models using zero-offset vertical seismic profiling (vsp) data. *Geophysics*, **70**(2), F17–F25 (doi: 10.1190/1.1884827)

Voigt DE, Peters LE and Anandakrishnan S (2013) 'Georods': the development of a four-element geophone for improved seismic imaging of glaciers and ice sheets. *Annals of Glaciology*, **54**(64), 142–148 (doi: 10.3189/2013AoG64A432)

Wiechert E (1910) Bestimmung des weges der Erdbebenwellen im Erdinnern. I. theoretisches (Raypath determination of earthquakes waves in the Earth's interior, I. theory). *Physikalische Zeitschrift*, **11**, 294–304

Wingham DJ (2000) Small fluctuations in the density and thickness of a dry firn column. *Journal of Glaciology*, **46**(154), 399–411 (doi: 10.3189/172756500781833089)

APPENDIX

This is a derivation of Equation 5 seen in the text. Here superscripts denote rays, and subscripts denote quasi-layers in the firn; e.g. t_2^B is the time ray B spends in layer 2, and Q_2 is the quality factor in that layer. m^B, A is the gradient obtained from the logarithm of the spectral ratio $S^B(f)/S^B(A)$, where $S^B(f)$ is the spectrum of a wavelet following the path of ray B, and $S^A(f)$ is the spectrum of a wavelet following the path of ray A. Figure 4a shows two rays A and B, which reach the bottom of firn quasi-layers 1 and 2, with quality factors Q_1 and Q_2, respectively. These rays would be used to calculate Q in the interval between their maximum penetration depths, i.e. Q_2. The difference in their attenuated times is:

$$\begin{aligned} t^{*B,A} &= t^{*B} - t^{*A} \\ &= \left(\frac{t_1^B}{Q_1} + \frac{t_2^B}{Q_2}\right) - \frac{t_1^A}{Q_1}. \end{aligned} \tag{A.1}$$

Assuming Q_1 is known, rearranging for Q_2 gives:

$$Q_2 = t_2^B \bigg/ \left[t^{*B,A} + \frac{t_1^A - t_1^B}{Q_1} \right]$$

$$= t_2^B \bigg/ \left[\frac{-\pi}{m^{B,A}} + \frac{t_1^A - t_1^B}{Q_1} \right], \tag{A.2}$$

from substitution of $m = -\pi\delta t/Q$. Consider a ray C which penetrates to the base of a third layer; by a similar argument,

$$Q_3 = t_3^C \Bigg/ \left[\frac{-\pi}{m^{C,B}} + \frac{t_1^B - t_1^C}{Q_1} + \frac{t_2^B - t_2^C}{Q_2} \right] \tag{A.3}$$

To calculate Q_n in an arbitrary layer n, we would use the spectral ratio gradient calculated from two rays X and Y, one of which (Y) has penetrated to the base of layer n, and one of which (X) has penetrated to the base of layer $n-1$. By extension of equation (A.3), Q_n is:

$$Q_n = t_n^Y \Bigg/ \left[\frac{-\pi}{m^{Y,X}} + \sum_{i=1}^{n-1} \frac{t_i^X - t_i^Y}{Q_i} \right]. \tag{A.4}$$